The hepatocyte traffic network in the human hepatitis A virus biological cycle from an evolutionary perspective

Check for updates

Albert Carcereny [1,4], Alba Arrebola [1,4], Gemma Chavarria-Miró[1,4], Montserrat de Castellarnau[1], Cristina Fuentes[1], David Garcia-Pedemonte[1], Adán Martínez-Velázquez[1], Enric Ribes[2], Albert Bosch[1], Susana Guix[1], Maria Isabel Costafreda[1,3] & Rosa M. Pintó [1,3] ✉

Hepatitis A virus (HAV) egresses from hepatocytes cloaked in exosomes (eHAV). However, the traffic network used for its release from polarized hepatocytes is not completely understood. We propose that eHAV biogenesis may follow not only an ESCRT-mediated pathway but also the syndecan-syntenin-ALIX pathway. The Bro1 and the V domains of ALIX bind to the pX extension of VP1 and the VP2-late domains of the unmature capsid, respectively. A Serine-to-Glycine replacement at position 134 of VP2, closely located with the first late domain, facilitates the interaction with ALIX promoting the syndecan-syntenin-ALIX pathway and improving the basolateral egress, preferentially using RAB35. This replacement is conserved in hepatoviruses infecting a wide range of mammalian species, but not in hepatoviruses infecting chimpanzees and humans. An inefficient basolateral egress could be a strategy to escape the antiviral cellular response in apes.

Hepatitis A virus (*Hepatovirus ahepa*, HAV) exists in a dual phenotype: as naked particles and as quasi-enveloped viruses. Particles egress hepatocytes inside exosome-like vesicles, giving rise to circulating quasi-enveloped particles (eHAV)[1]. Naked particles are released from the quasi-envelop during the gastrointestinal transit and are shed in feces[2].

Exosomes are a particular type of extracellular vesicles whose biogenesis involves the formation of intraluminal vesicles (ILV) into the multivesicular bodies (MVB), and their secretion via the MVB exocytic pathway[3–5]. ILVs are formed through an endosomal inward budding, usually in an endosomal sorting complex required for transport (ESCRT)-dependent or canonical manner, and during the process, different cargos are incorporated[6]. The canonical exosome biogenesis pathway involves the internalization of ubiquitinated proteins through their direct interaction with the ESCRT-0, -I, and -II complexes[7]. Alternatively, syntenin binds syndecan through its tandem PDZ domains[8], and apoptosis-linked-gene-2-interacting-protein-X (ALIX), an ESCRT-III-binding protein, through its "late domain" motifs[9], directing the syndecan cargos into ILVs. This latter pathway is known as the syndecan-syntenin-ALIX-exosome biogenesis[9]. In its turn, ALIX harbors a Bro1 domain, which interacts with the ESCRT-III CHMP4 protein, and a central V-shaped domain, which interacts with (L) YPXnL-"late domain" bearing proteins, such as syntenin and G-protein-

coupled-receptor-proteinase-activated-receptor 1[9–11]. Also, many retroviruses harbor this type of "late domain" motifs, and their interaction with ALIX acts in the budding process[12–19].

The eHAV particles contain many common exosome-associated proteins and multiple endosomal sorting complex required for transport III (ESCRT-III) associated proteins, such as CHMP1A, CHMP1B, CHMP4B, IST1, and ALIX[20]. In addition, syntenin has also been detected in the eHAV particles[20], which, combined with the essential role of ALIX in the eHAV release, suggests a role for the syndecan-syntenin-ALIX pathway. Accordingly, HAV has two tandem YPX₃L "late domains" in the VP2 capsid protein, at positions 144-149 (YPHGLL) and 177-182 (YPVWEL)[1]. Despite being buried in the mature capsid, these "late domains" have been proven to redundantly function during quasi-envelopment and eHAV release[21], suggesting a higher accessibility in the immature capsid budding into the MVBs[21,22]. ALIX may exist as monomers and dimers, being the dimeric form the active one interacting with the ESCRT-III CHMP4 protein[23]. This dimeric conformer with two functional V domains would enable dual interaction with syntenin and immature capsids, respectively. However, how they are loaded into the MVB is yet not fully understood.

Additionally, the immature HAV capsid contains the unprocessed VP1-pX protein, with three potentially ubiquitylation sites in the pX

---

[1]Enteric Virus Laboratory, Department of Genetics, Microbiology and Statistics, School of Biology, and Institute of Nutrition and Food Safety, University of Barcelona, Barcelona, Spain. [2]Enteric Virus Laboratory, Department of Cell Biology, Physiology and Immunology, School of Biology, University of Barcelona, Barcelona, Spain. [3]Centro de Investigación Biomédica en Red de Enfermedades Hepáticas y Digestivas (CIBERehd), Instituto de Salud Carlos III, Madrid, Spain. [4]These authors contributed equally: Albert Carcereny, Alba Arrebola, Gemma Chavarria-Miró. ✉e-mail: rpinto@ub.edu

Fig. 1 | Expression of genes coding for proteins involved in exosome biogenesis and trafficking in human hepatocytes. A mRNA levels from genes coding for ALIX, HD-PTP, TSG101, syntenin-1, and syndecan 1 in the Huh7-A-I cell line. **B** mRNA levels from genes coding for RAB7A, RAB11A, RAB11C, RAB27A, RAB27B, and RAB35 in the Huh7-A-I cell line. Dots correspond to n = 6 independent biological replicates. Each biological replicate was twice titrated, and the average is shown in the depicted values.
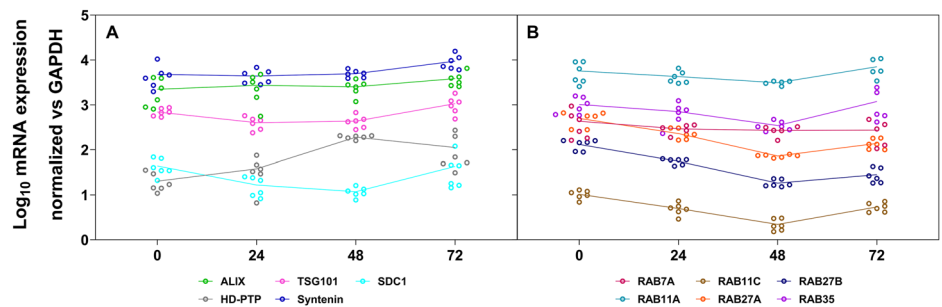
protein[2]. Ubiquitylation is a common signal for cargo recruitment to MVBs through the action of ALIX, tyrosine-protein phosphatase non-receptor type 23 (HD-PTP), and the ESCRT-0-I-II complexes[24,25]. However, the TSG101 subunit of ESCRT-I, which interacts with ESCRT-0 and ubiquitinated cargos, has not been found in eHAV[1]. In contrast, it has recently been described that the VP1-pX protein interacts in a non-redundant manner with the Bro1 domain of ALIX and HD-PTP, suggesting a role of the VP1-pX protein in the HAV quasi-envelopment[25].

Hepatocytes are multi-polarized cells with complex traffic pathways[26,27]. Basolateral membrane proteins undergo fast recycling directly from the early basolateral endosomes (BEE) or may be recycled via the subapical endosome compartment (SAC). Similarly, apical proteins are endocytosed in apical early endosomes and sorted into the apical recycling endosome (ARE). Additionally, proteins in the BEE, ARE, and SAC compartments may be sorted to the MVB and further to the lysosome for degradation. In polarized colon carcinoma cells, different populations of exosomes are released from apical and basolateral cell surfaces[28], suggesting the existence of selective mechanisms controlling the cargo sorting into different vesicles[29]. Furthermore, RAB proteins regulate the intracellular traffic pathways between the endocytic compartments and the exosome release through different membranes[5]. Exosome secretion is promoted among others by RAB11, RAB27, RAB35, and RAB7 proteins[3–5], the latter being involved in the secretion of syndecan-syntenin-ALIX-containing exosomes in breast tumor cells[9]. However, although the RAB7A isoform is enriched in eHAV exosomes, its depletion has no effect on virus release[20]. Similarly, depletion of RAB7 in HeLa cells does not inhibit exosome release[30]. Remarkably, RAB11A-containing recycling endosomes are required for bile canalicular formation[31]. It has been proven that HAV egresses from hepatocytes from both the basolateral and apical membranes in the eHAV form[32]. However, whether there are different compartments for eHAV biogenesis, and/or differences in the traffic pathway for its egress, is yet to be elucidated.

In this work, we focused on the use of the canonical ESCRT-mediated and the syndecan-syntenin-ALIX-mediated exosome biogenesis pathways by two HAV strains differing in their replication capacity: the HM-175 strain (L0)[33], and a fast-replicating HM-175-derived strain (HP)[34]. HP harbors a mutation in the VP2 protein, which might facilitate the accessibility of one of the late domains. The eHAV secretion pattern in polarized hepatocytes, and its relationship with traffic pathways controlled by different RAB proteins was analyzed. An evolutionary origin for the preferential apical release of human HAV is proposed.

Results

Expression of genes involved in exosome biogenesis and secretion pathways in Huh7-A-I cells

The expression of genes involved in the ESCRT-mediated and syndecan-syntenin-ALIX-mediated exosome biogenesis pathways was analyzed in the human hepatocarcinoma-derived Huh7-A-I cell line[35]. Expression of genes coding for ALIX (Programmed Cell Death 6 Interacting Protein; PDCD6IP gene), HD-PTP (Protein Tyrosine Phosphatase Non-Receptor Type 23; PTPN23 gene), TSG101 (tumor susceptibility gene 101 protein; TSG101

gene), syntenin-1 (syndecan binding protein 1; SDCBP gene) and SDC1 (syndecan 1; SDC1 gene) was measured during 72 h. The mRNA levels were normalized vs the expression of GAPDH (glyceraldehyde-3-phosphate dehydrogenase; GAPDH housekeeping gene). Overall, SDCBP gene expression was the highest, followed by ALIX-coding gene, TSG101, HD-PTP, and SDC1 (Fig. 1A).

Additionally, expression of genes coding for several Ras-related proteins involved in exosome secretion (RAB7A, RAB11A, RAB11C, RAB27A, RAB27B, and RAB35) was also ascertained. The mRNA levels of RAB11A were found to be the highest, followed by RAB35 (Fig. 1B).

These results suggest that not only the canonical ESCRT-mediated pathway but also the syndecan-syntenin-ALIX-mediated exosome biogenesis may be active in Huh7-A-I cells, and that RAB11A and RAB35 could be involved in its secretory pathway.

Effect of HAV infection on the expression of genes involved in the exosome biogenesis pathways and their secretion

To elucidate whether the expression pattern of genes involved in the exosome biogenesis pathways and the associated RABs varies during the infection cycle, Huh7-A-I cells were infected with the L0 or the HP strains using a multiplicity of infection (MOI) of 5.

Virus replication was confirmed by quantifying the genome copy (GC) numbers in the supernatant of infected cells at 0, 24, 48, and 72 h post-infection (p.i.). The GC fold increase of the HP strain was significantly higher compared to the L0 strain, confirming its faster replication rate (Fig. 2A). Concomitantly, the mRNA levels of genes involved in the ESCRT-mediated (Fig. 2B–D) and the syndecan-syntenin-mediated (Fig. 2B, E, F) exosome biogenesis pathways were measured in HAV-infected vs mock-infected cells. A minimum of a 2-fold increase was established as a cutoff level to define a specific rise. HAV infection was associated with a moderate, although sustained, increase of ALIX-coding gene expression in both L0- and HP-infected cells up to 48 h p.i. (Fig. 2B). But in this latter case, the increase was significantly higher (3-fold vs 2-fold). HD-PTP, TSG101, SDCBP, and SDC1 gene expression did not show specific increases (Fig. 2C–F).

Additionally, the expression pattern for RAB7A, RAB11A, RAB11C, RAB27A, RAB27B, and RAB35 coding genes was analyzed (Fig. 2G–J and Supplementary Fig. 1). The mRNA levels for RAB7A were higher in HP-infected cells than in L0-infected cells at 48 h p.i. (Fig. 2G). The mRNA levels for RAB35 increased at 72 h p.i. in HP-infected cells (Fig. 2J). In all cases, the increases were modest.

These results suggest that HAV quasi-envelopment may be mediated not only by the ESCRT pathway, involving ALIX, HD-PTP, and TSG101, but also through the syndecan-syntenin-ALIX pathway, involving ALIX, syntenin-1, and syndecan 1, with RAB7A and RAB35 being used for their secretion.

The role of ALIX, HD-PTP, and syntenin-1 in the biogenesis of eHAV particles from L0 and HP strains

In the ESCRT-mediated exosome biogenesis pathway, ALIX and HD-PTP recruit capsids through their Bro1 domain, which in turn interacts with the ESCRT-0 STAM2 and the ESCRT-III CHMP4 proteins[25]. In the syndecan-
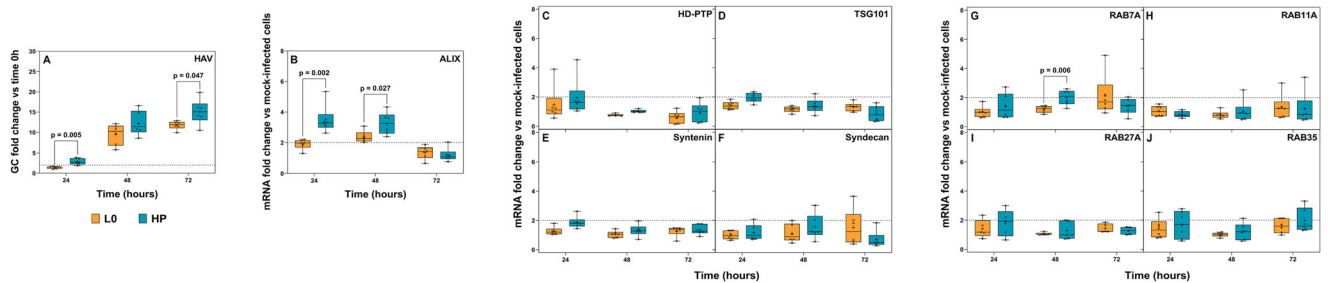
Fig. 2 | Effect of HAV replication on the expression of genes coding for proteins involved in exosome biogenesis and trafficking in human hepatocytes. A Genome copy fold increase over time in the supernatant of Huh7-A-I-infected cells with HAV strains L0 (orange) and HP (cyan). mRNA fold-changes of ALIX (**B**), HD-PTP (**C**), TSG101 (**D**), Syntenin-1 (**E**), Syndecan 1 (**F**), RAB7A (**G**), RAB11A (**H**), RAB27A (**I**), and RAB35 (**J**) of HP and L0 Huh7-A-I-infected cells. Box diagrams represent the 25th, 50th, and 75th percentiles with whiskers towards the minimum and maximum values, black crosses represent the mean. Dots correspond to $n = 6$ biological replicates. Each biological replicate was twice titrated, and the average is shown in the depicted values. The dashed line depicts the cutoff level established at a 2-fold change. Statistically significant differences between L0 and HP strains are depicted.

syntenin-mediated eHAV biogenesis pathway, ALIX would play a role connecting capsids and syntenin-1, which would, in turn, interact with syndecan 1.

Co-localization analysis of ALIX and HAV in infected Huh7-A-I cell monolayers (MOI = 5) was performed using confocal microscopy. At 48 h p.i., capsid antigen was already visible in L0-infected cells (Fig. 3A), although it was much more extensive and intense in HP-infected cells (Fig. 3G), confirming again the HP fast-growing phenotype. Remarkably, ALIX was also more abundant in HP-infected cells than in L0-infected cells at 48 h p.i. (Fig. 3H vs Fig. 3B), in accordance with the increase of its mRNA levels (Fig. 2B). Similarly, ALIX increased in L0-infected cells from 48 to 72 h p.i. (Fig. 3B, E). A clear co-localization between ALIX and capsid antigens from both strains was observed, being more intense with the HP capsids compared to L0 capsids (Fig. 3I vs Fig. 3C, and Fig. 3L vs Fig. 3F). To measure the magnitude and intensity of the co-localization between ALIX and capsids from the L0 and HP strains, quantitative analyses were performed at 72 h p.i. (Fig. 3M), revealing a significantly higher ($p = 0.010$) proportion of HP capsids co-localizing with ALIX (M1) than L0 capsids. These results point to more capsids of HP interacting with ALIX compared with L0. To further confirm this observation, we tested the capacity of an anti-ALIX polyclonal antibody to pull down L0 and HP capsids compared with a monoclonal anti-HAV antibody. The anti-ALIX antibody was able to pull down 28.50% and 55.31% of L0 and HP capsids, respectively, compared with capsids immunoprecipitated with the anti-HAV antibody (Fig. 3N), this difference being statistically significant ($p = 0.002$). Using the described 3D structure of HAV[22] to locate the two point mutations differentiating L0 and HP capsids (S2134G and L1123F), we found that the replacement S134G in VP2 was located at 4.5 Å from the Y of the 144YPHGLL149 late domain, while the L123F replacement in VP1 was located far from any of the two late domains (Supplementary Fig. 2). Since a Gly residue is much more flexible than a Ser residue, we hypothesized that the VP2 S134G replacement could facilitate the interaction between the first late domain in HP capsids and the ALIX V domain.

To evaluate the role of ALIX in the eHAV release, we studied the effect of ALIX-coding gene silencing on the virus release. A significant decrease in ALIX mRNA levels was achieved (reduction of 85.35% ± 1.55%), which correlated with a notable decrease in the protein detection in western blots (Supplementary Fig. 3). ALIX silencing resulted in a significant increase ($p < 0.001$) of the ratio between the total intracellular genomes and the total infectious viruses in the supernatant of L0-infected cells, which is a measure of the decrease in virus release, (Fig. 3O and Supplementary Fig. 4). However, HP release was not affected by ALIX silencing (Fig. 3O), which contrasts with its stronger co-localization with ALIX and more efficient immunoprecipitation with an anti-ALIX antibody, compared with L0. These results could be explained by the stimulation of ALIX expression in HP-infected cells that could balance the silencing effect, combined with a greater affinity binding of HP capsids with ALIX.

To assess the consequences of the differential interaction of L0 and HP with ALIX in the actual release of viruses into the supernatants of Huh7-A-I-infected cells, the ratio of eHAV to naked HAV particles was analyzed by isopycnic gradient ultracentrifugation. Although in both strains most genomes banded at the density of eHAV particles, the proportion of genomes banding at the density of naked particles was significantly lower in the supernatants of HP-infected cells (Supplementary Fig. 5 and Supplementary Table 1). The mechanism of naked HAV particle release remains to be elucidated, but it has been proposed that they originate from the lysis of eHAV particles[2]. In fact, some broken empty exosomes were observed in the low–density fractions, and many HP-derived naked particles remained attached to them (Supplementary Fig. 5G). Consequently, the lower proportion of naked particles in supernatants from HP-infected cells may be the result of a tighter interaction of HP virions with exosome components. After ALIX silencing, most of the egressed particles remained quasi-enveloped, in both strains (Supplementary Fig. 6). The proportion of particles in the supernatant of silenced cells was lower than in non-silenced cells for L0 but not for HP, and the proportion of naked particles increased, particularly for the HP strain (Supplementary Fig. 6), likely indicating a weaker interaction in conditions of ALIX reduction.

Confocal microscopy analyses were also performed to explore the co-localization of L0 and HP capsids with HD-PTP and syntenin-1, as markers of the canonical ESCRT pathway and the syndecan-syntenin-ALIX pathway, respectively. Overall, both L0 and HP capsids showed significantly ($p < 0.001$) lower co-localization with HD-PTP than with syntenin-1 (Fig. 4A–D). Both co-localized equally with HD-PTP (Fig. 4A, B), with similar proportions of co-localizing capsids (7% and 6%, respectively). Instead, significantly higher proportions of HP capsids (19%) co-localized with syntenin-1 compared with L0 capsids (13%) (Fig. 4C, D), which may suggest a facilitated interaction of HP with syntenin-1 through its stronger interaction with ALIX. We tested the effect of HD-PTP and syntenin-1 gene silencing on the co-localization of capsids. Silencing of both genes induced a significant reduction of the proportion of L0 and HP capsids co-localizing with both markers (Fig. 4A–D). Specifically, HD-PTP knockdown induced significant reductions in the proportion of capsids co-localizing with HD-PTP from 7% to 1% (L0) and from 6% to 2% (HP) (Fig. 4B). Similarly, syntenin-1 silencing caused significant declines on the co-localization of L0 and HP capsids with syntenin-1 from 13% to 9% and from 19% to 13%, respectively (Fig. 4D). Remarkably, while HD-PTP gene silencing did not show any effect on the cross co-localization with syntenin-1 (Fig. 4C, D), syntenin-1 gene silencing did induce an increase in the co-localization of HP capsids with HD-PTP from 6% to 11% but not of L0 capsids (Fig. 4A, B), suggesting a more important role of syntenin-1 in HP release.

The effect of HD-PTP and syntenin-1 gene silencing on virus release was analyzed. Significant decreases in HD-PTP and syntenin-1 mRNA levels were achieved (reduction of 71.94% ± 0.04% and 92.75 ± 1.52%), which correlated with important reductions in protein detection in western
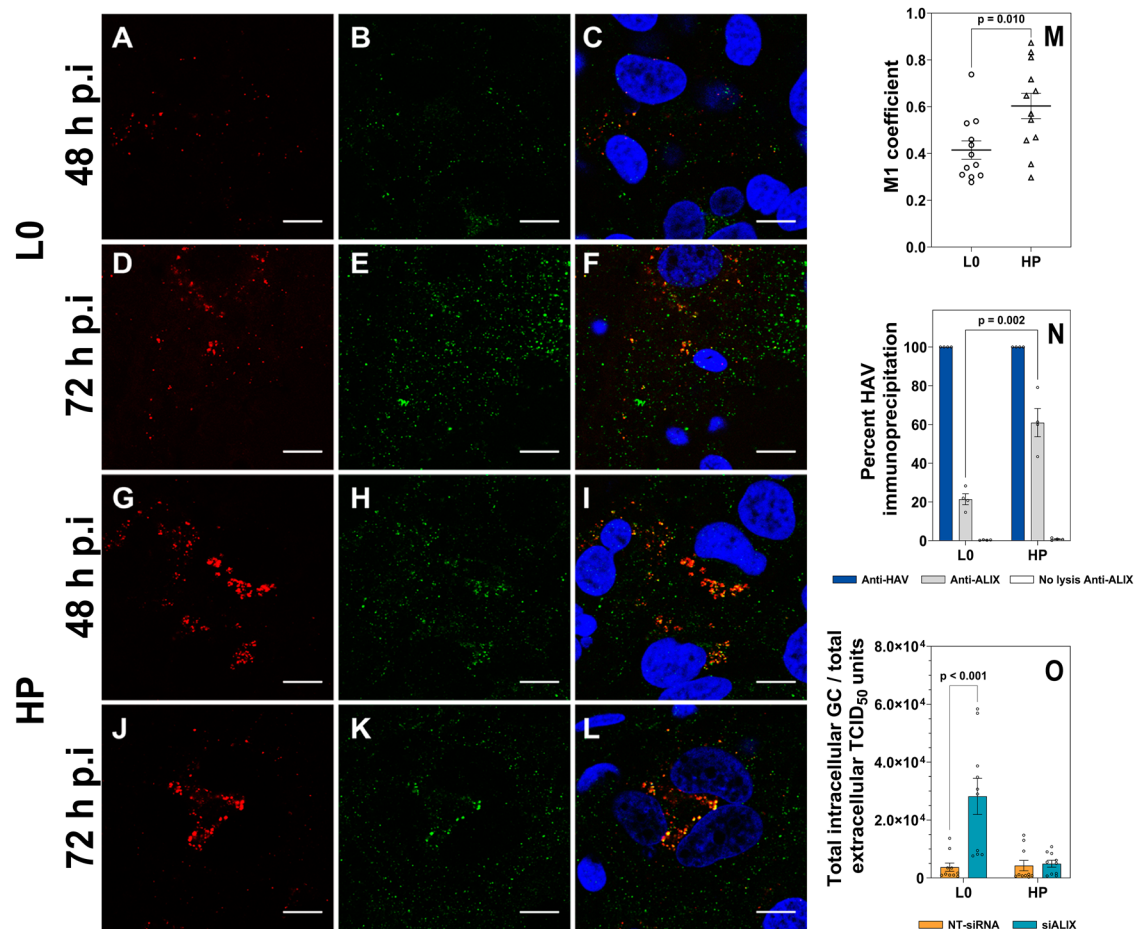
Fig. 3 | ALIX interaction with HAV capsids. A–L Co-localization of ALIX and HAV capsids in Huh7-A-I-infected cells. **A–F** correspond to L0-infected cells, and **G–L** to HP-infected cells. **A** Indirect immunofluorescence (IIF) of L0 capsids at 48 hours post-infection (h p.i.). **B** IIF of ALIX at 48 h p.i. **C** Co-localization of L0 capsids and ALIX at 48 h p.i.; red and green fluorescence correspond to HAV capsids and ALIX, respectively; orange to yellow fluorescence depicts co-localization of capsids and ALIX. Similarly, **D–F** depict the same analysis in L0-infected cells at 72 h p.i. (**G–I**) in HP-infected cells at 48 h p.i., and (**J–L**) in HP-infected cells at 72 h p.i. The white bar corresponds to 10 μm. **M** Quantitative confocal microscopy analysis of the proportion of HAV capsids co-localizing with ALIX (M1 coefficient) at 72 h p.i. Dots correspond to the M1 value of each of $n = 12$ images from $n = 3$ independent biological replicates. The total number of infected cells counted was 51 and 77 for L0 and HP, respectively. Significant differences between L0 and HP-infected cells are depicted. **N** Immunoprecipitation of L0 and HP naked capsids, released from

exosomes by freeze-thaw cycles combined with sonication, with an anti-HAV antibody (blue) and an anti-ALIX antibody (gray). The percentage of capsids pulled down with the anti-ALIX antibody is expressed relative to the percentage of capsids pulled down with the anti-HAV antibody. As a control, no lysed particles were pulled down with the anti-ALIX antibody (white). Data represent the mean ± standard error of $n = 4$ independent biological replicates. Significant differences are depicted. **O** Effect of ALIX-coding gene silencing on HAV egress. The ratio between the total intracellular genomes and the total number of infectious viruses, expressed in $TCID_{50}$, in the supernatant, is shown. NT-siRNA and siALIX columns represent the effect of silencing using a mixture of non-target siRNAs and a mixture of siALIX RNAs, respectively. A silencing effect on HAV egress should induce an increase in this ratio. Data represent the mean ± standard error from $n = 10$ biological replicates. Each biological replicate included two technical replicates, whose average is depicted.

blots (Supplementary Fig. 3). Silencing of both genes resulted in significant increases in the ratio of the total intracellular genomes to the total infectious viruses in the supernatant (Fig. 4E and Supplementary Fig. 4). Curiously, the effect of HD-PTP knockdown in decreasing L0 release was stronger in comparison with the effect of syntenin-1 silencing (Fig. 4E), suggesting a preference for the ESCRT pathway for L0 release. In contrast, no differences were observed in the decrease of HP release depending on HD-PTP or syntenin-1 silencing (Fig. 4E). Yet, the increase in HP co-localization with HD-PTP observed after syntenin-1 knockdown (Fig. 4B) suggests a corrective communicating-vessels effect and points to a more relevant role of the syndecan-syntenin-ALIX pathway for HP release.

The role of RAB GTPases in eHAV secretion from L0- and HP-infected cells
To identify whether RAB7A and RAB35 (whose gene expression was moderately increased during HAV infection Fig. 2G, J), and RAB11A (whose coding gene was highly expressed Fig. 1B), were involved in eHAV

release from Huh7-A-I cells, confocal microscopy analyses were performed after infecting cells with a MOI of 5 for 72 h (Fig. 5). Overall, both L0 and HP capsids similarly co-localized with all RABs (Fig. 5A). Specifically, the average proportion of capsids co-localizing with RAB7A, RAB11A and RAB35 was 24%, 21% and 20%, respectively for L0, and 21%, 18% and 23% for HP (Fig. 5B). Despite a lack of significance, a tendency of HP capsids to show higher co-localizations with RAB35 compared with L0 capsids was observed (Fig. 5B). To assess whether RAB7A, RAB11A and RAB35 could promote HAV release, a series of individual and double gene silencing experiments were performed. The individual gene silencing achieved was 97.74% ± 0.36%, 88.51% ± 1.20% and 67.96% ± 2.27% regarding mRNA reduction, and around 92%, 75% and 84% regarding protein reduction, for *RAB7A*, *RAB11A* and *RAB35*, respectively (Supplementary Fig. 3). Individual RAB7A and RAB11A silencing did not induce significant increases in the ratio of the total intracellular GC vs the total infectious viruses in the supernatant for the L0 strain, and only a minimum effect on HP (Fig. 5C and Supplementary Fig. 7), indicating a minor effect on HAV release. The most
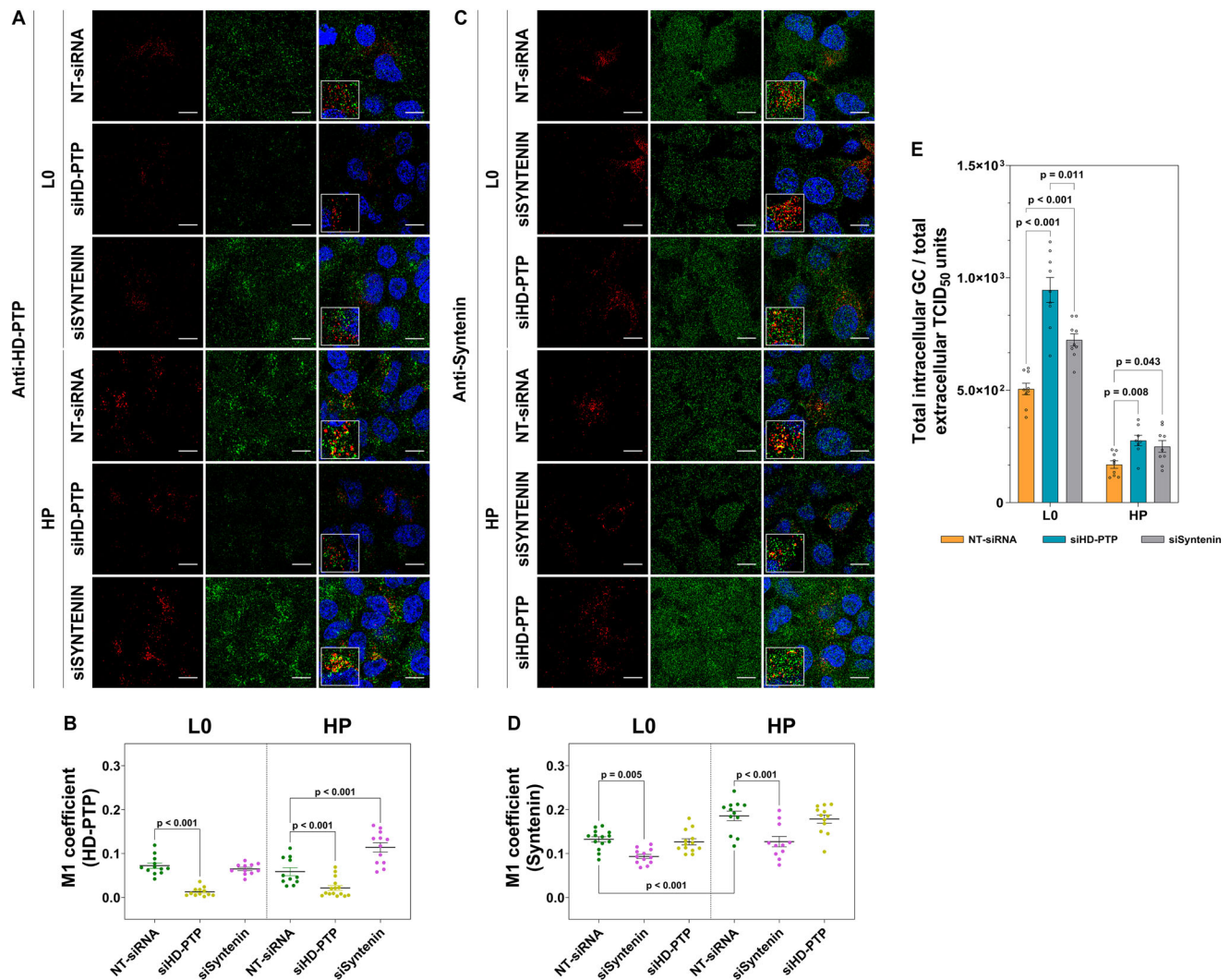
Fig. 4 | Role of syntenin-1 and HD-PTP in the HAV release from Huh7-A-I-infected cells. **A** Effect of HD-PTP and syntenin-1 coding gene silencing on the co-localization of L0 and HP capsids with HD-PTP; at 24 h p.i. capsids were immunolabelled in red, and HD-PTP in green. **B** Quantitative analysis of the proportion of HAV capsids co-localizing with HD-PTP (M1) in non-silenced (NT-siRNA) and knock-down cells for HD-PTP (siHD-PTP) and syntenin-1 (siSyntenin-1). **C** Effect of syntenin-1 and HD-PTP coding gene silencing on the co-localization of L0 and HP capsids with syntenin-1; at 24 h p.i. capsids were immunolabelled in red, and syntenin-1 in green. **D** Quantitative analysis of the proportion of HAV capsids co-localizing with syntenin-1 (M1) in non-silenced (NT-siRNA) and knock-down cells for syntenin-1 (siSyntenin-1) and HD-PTP (siHD-PTP). The confocal images (**A, C**)

layout is as in Fig. 3. The white bar corresponds to 10 μm. Quantitative analyses (**B, D**) were done using an average of $n = 12$ images, from $n = 2$ independent biological replicates. The total number of infected cells counted was in the range of 46-116 and 67-154 for L0 and HP, respectively. Šidák correction was applied in the multiple comparison test. **E** Effect of HD-PTP and syntenin-1 coding gene silencing on the ratios between the intracellular genomes and the infectious titers in the supernatant, as a measure of HAV release. Dunnett T3 (L0) and Tukey (HP) corrections were applied in the multiple comparison test. Data represent the mean ± standard error from $n = 9$ independent biological replicates. Each biological replicate included two technical replicates, whose average is depicted. Significant differences are shown.

striking finding was the increase in the ratio of total intracellular GC to total infectious viruses in the supernatant during RAB35 silencing, which indicates a reduction in virus release (Fig. 5C and Supplementary Fig. 7). On average, increases of 1.75X and 3.50X for L0 and HP, respectively, were observed. This stronger effect on the HP egress could also be inferred with the double RAB7A and RAB11A silencing (96.00% ± 1.36% and 74.36% ± 3.36% mRNA reduction, respectively), which induced an increase in RAB35 gene expression (Supplementary Table 2), and concomitantly a decrease in the ratio of intracellular GC to infectious virus in the supernatant, which indicates an increase of release (Figs. 5C and S7). In contrast, for L0, this double silencing induced an increase in the ratio of intracellular GC to infectious virus in the supernatant, which may indicate a certain role of these RABs, despite their minor individual effect, in L0 egress (Fig. 5C and Supplementary Fig. 7). The effect of RAB11A knockdown on L0 egress was intriguing (Fig. 5C and Supplementary Fig. 7), since a decrease in the ratio of

intracellular GC vs the infectious virus in the supernatant indicates a more efficient release. This result may be explained by the significant rise of RAB7A mRNA (Supplementary Table 2), suggesting that L0 may indeed use RAB7A for its egress. Although this reasoning is contradictory with the lack of effect of RAB7A silencing, the existence of a communication-vessel effect between the network of RAB GTPases could neutralize the knockdown outcome.

The eHAV trafficking pathway in polarized hepatocytes

Differentiation of Huh7-A-I cells was promoted by growing them for 14 days in the presence of DMSO. Polarization of monolayers was confirmed by confocal microscopy (Fig. 6A, B) after staining with antibodies directed against specific markers of the apical (AP) tight junction (zonula occludens-1: ZO-1) and basolateral (BL) membranes (alpha 1 Sodium Potassium ATPase: Na+K+-ATPase). Monolayers of columnar polarized
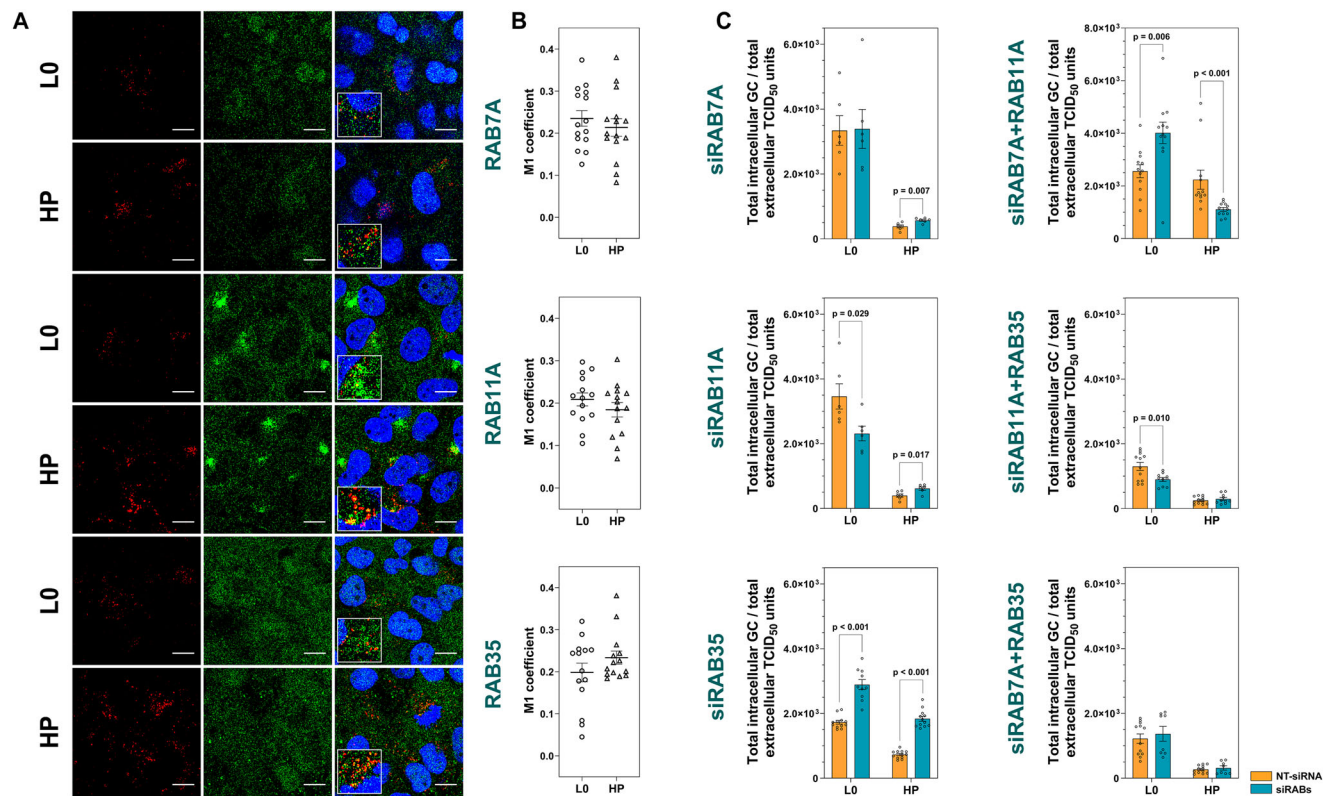
Fig. 5 | Interaction of RAB proteins with HAV capsids. A Co-localization of HAV capsids and RAB proteins in Huh7-A-I-infected cells. At 72 h p.i., L0 and HP capsids were immunolabelled in red and RAB proteins in green. The confocal images layout is as in Fig. 3. The white bar corresponds to 10 μm. **B** Quantitative microscopy analysis of the proportion of HAV capsids co-localizing with RAB7A, RAB11A, and RAB35, respectively, was done using $n = 14$ images, from $n = 3$ independent biological replicates. The total number of infected cells counted was in the range of 43-48 and 85-124 for L0 and HP, respectively. **C** Effect of single and double RAB coding genes silencing on the ratios between the intracellular genomes and the infectious titers in the supernatant, as a measure of HAV release. Data represent the mean ± standard error of $n = 6$ independent biological replicates for RAB7A and RAB11A and $n = 12$ independent biological replicates in the rest of the experiments. Each biological replicate included two technical replicates, whose average is depicted. Significant differences are shown.

cells were formed (Fig. 6B), showing very low levels of permeability (Fig. 6C).

Virus egress from the BL and AP membranes of polarized Huh7-A-I cells grown on transwells was investigated. First, transcytosis of both L0 and HP strains, from either side BL-AP and AP-BL was tested for up to 3 h, and a few percent of virions (from below the limit of detection to 4%) passed through the cells (Fig. 6D). The egress of both L0 and HP strains mostly occurred through the AP membrane (Fig. 6E). However, while no significant differences were found between the egress of HP viruses through the AP and the BL membranes, the BL egress of L0 viruses, at 5 and 7 days p.i., was significantly lower than the AP egress (Fig. 6E).

The involvement of RAB GTPases in the complex hepatocyte trafficking network could mediate the vectorial release of eHAV. The differential connection of RAB proteins with the BL and AP membranes was analyzed to dissect eHAV egress. RAB7A, RAB11A, and RAB35 co-localized with markers of both the basolateral (Fig. 7A–F), and apical (Fig. 7G–L) membranes. With the aim of estimating the differential localization of each RAB, we performed quantitative analysis (Fig. 7M–R). We found that the proportion of the BL and AP membranes co-localizing with RAB7A (Fig. 7M) and RAB11A (Fig. 7N) was similar, while the proportion of the BL membrane co-localizing with RAB35 was significantly higher than the corresponding proportion of the AP membrane (Fig. 7O), indicating a certain preference of RAB35 for the BL compartment. In contrast, the proportion of each RAB co-localizing with the BL membrane was significantly higher than the proportion co-localizing with the AP membrane (Fig. 7P–R), which may be explained by the largest surface of the BL membrane[36]. Altogether, these data suggest a specific involvement of RAB35

in the basolateral trafficking pathway, which could, in turn, determine the ratio of BL to AP eHAV egress.

Degree of conservation of the VP2 S134G replacement in hepatoviruses infecting small mammals, monkeys, apes, and humans

As stated above, only two amino acid replacements exist between the human hepatovirus strains L0 and HP: L123F in the VP1 protein and S134G in the VP2 protein. This last replacement could facilitate the interaction between the first late domain and the ALIX V domain in the HP strain, sequentially promoting the syndecan-syntenin-ALIX-exosome biogenesis at the BEE and their egress using RAB35. We wondered how conserved this position is along the different hepatoviruses described. The alignment of 132 VP2 sequences from 9 hepatovirus species infecting 34 different mammalian species revealed that hepatoviruses infecting humans and chimpanzees, except for the human-derived HP strain, have a Serine at position 134 of VP2, while the rest of hepatoviruses infecting monkeys, seals, rodents, hedgehogs, shrews, bats, and marsupials have a Glycine (Fig. 8). In contrast, no pattern was observed regarding the L123F replacement in the VP1 protein (Supplementary Fig. 8).

Discussion

Hepatocytes are unique multipolar epithelial cells, each participating in multiple lumina: the bile canaliculi, and the basal surfaces towards the endothelial lining[26]. HAV exists as naked particles, which are shed in feces, and as quasi-enveloped virions (eHAV), circulating in blood during infection[1].

ALIX has been described as critical for HAV release in exosome-like vesicles[1]. Exosome biogenesis may follow the canonical ESCRT-dependent[6]
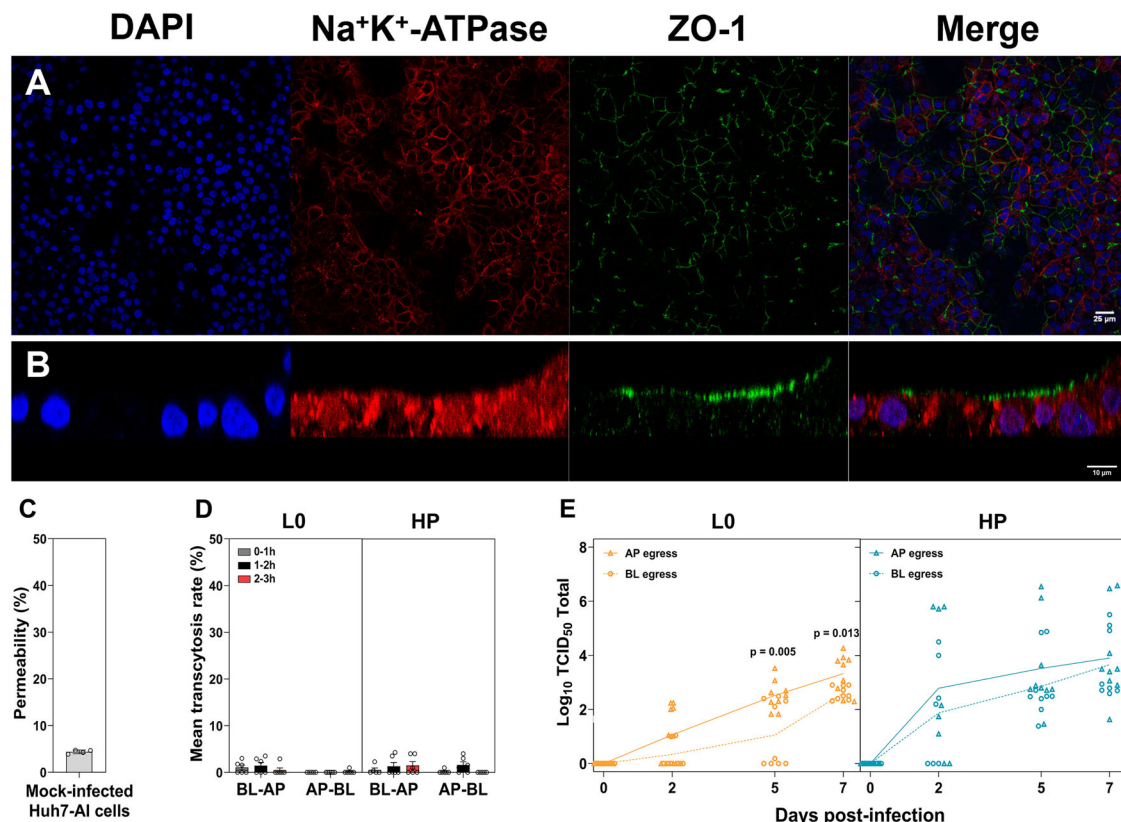
Fig. 6 | Vectorial release of HAV from polarized hepatocytes. A IIF of polarized Huh7-A-I cells using antibodies directed against the Na^+K^+ ATPase (green) and ZO-1 (red), markers of the basolateral (BL) and apical (AP) membranes, respectively. Nuclei are blue labeled. Images are in the axial plane. **B** Same images in the sagittal plane. White bars in (**A**, **B**) correspond to 25 µm and 10 µm, respectively. **C** Permeability of 4 kDa FITC-dextran through the monolayer of polarized Huh7-A-I; data represent the mean ± standard error of $n = 4$ independent biological replicates. **D** Mean transcytosis rates estimated at hourly intervals at 37 °C using a MOI of 5. BL-AP: percent of viruses released into the AP chamber after being added to the BL membrane. AP-BL: percent of viruses released into the BL chamber after being added to the AP membrane. Data represent the mean ± standard error of the percentage of input virus from $n = 6$ independent biological replicates, including each 2 $TCID_{50}$ titrations, whose average is shown. **E** Total virus released from the AP and BL membranes in basolateral-infected polarized Huh7-A-I cells. Data represent the mean ± standard error of $n = 9$ independent biological replicates, including each 2 $TCID_{50}$ titrations, whose average is shown. Significant differences between the egress through the AP and BL membranes are depicted.

and the syndecan-syntenin-ALIX-mediated pathways[9]. While the canonical pathway has been proven to be used for eHAV release[25], the role of the syndecan-syntenin-ALIX-mediated pathway has not been elucidated, despite syntenin has been found in eHAV particles[20]. To bring some light on the additional use of this alternative pathway, we studied the expression of genes coding for key proteins involved in both pathways and of RAB GTPases that could mediate the MVB trafficking to the plasma membrane, in the Huh7-A-I hepatoma cells, which are permissive and highly robust for HAV replication[35]. Syntenin-1 mRNA levels were very high, in accordance with data previously reported in hepatoma cells[37], while the levels for ALIX, HD-PTP, and TSG101 were gradually lower. Nonetheless, antigen levels did not significantly differ, suggesting that both pathways are active in this hepatoma model. Additionally, RAB11A mRNA levels were very high, as expected due to its involvement in hepatocyte polarization[31], followed by RAB35 levels.

The cell response to the HP infection resulted in moderate to low fold-increases of mRNA levels for ALIX, HD-PTP, TSG101, and syntenin-1, while the response to L0 infection was very low, mostly reflecting the higher replication capacity of the HP strain. Additionally, ALIX silencing induced a decrease of L0 egress but not of HP, which can be explained by the counter-effect of the higher increase of ALIX-coding gene expression induced by the HP infection, and by the stronger interaction of HP capsids with ALIX. It has been described that the HAV pro-capsids interact with ALIX through the pX extension of VP1, which is identical in both L0 and HP, with the Bro1 domain of ALIX[25]. But additionally, two late domains have been identified in the HAV capsids[1], which, despite being buried in the mature capsid[22], have been proven to function redundantly during HAV egress[21]. An explanation could rely on a different structure of the intracellular capsids sorted into the exosomes, comparatively with naked extracellular capsids used in crystallographic analysis[22]. Indeed, the VP2 S134G replacement in the HP capsids could permit better accessibility of the Tyr at position 144 of the first VP2 late domain (144YPX₃L149), facilitating its interaction with the ALIX V domain. The side chain of Tyr of retrovirus YPX$_n$L late domains has the most distinctive interaction with ALIX[15].

To further dissect the eHAV biogenesis, a series of confocal microscopy analyses was performed to identify the co-localization of L0 and HP capsids with HD-PTP and syntenin-1, as markers of the ESCRT-mediated and the syndecan-syntenin-ALIX-mediated exosome biogenesis pathways, both in normal or protein-depleted conditions. Co-localization with syntenin-1 was stronger than co-localization with HD-PTP, particularly in the case of HP capsids. Interestingly, in syntenin-1-depleted cells, the co-localization of HP capsids with HD-PTP increased, but not the co-localization with L0 capsids, while in HD-PTP-depleted cells, the co-localization with syntenin-1 remained unaltered. The analysis of eHAV release after HD-PTP and syntenin-1 knockdown, revealed that both strains use both pathways. However, the L0 strain was more affected by HD-PTP silencing than the HP strain. Although no differences in the effect of HD-PTP and syntenin-1 on HP egress were detected, this could be the result of an increase in the use of HD-PTP as a compensatory measure, as proven through the co-localization analysis. In summary, in the hepatocyte Huh7-A-I model, L0 may

Fig. 7 | Distribution of RAB7A, RAB11A, and RAB35 GTPases along the basolateral and apical membranes of polarized Huh7-A-I cells.
A, C, E IIF of the BL membrane (Na⁺K⁺ ATPase marker in red) and RAB7A, RAB11, and RAB35, respectively (green). **B, D, F** Same images in the sagittal plane. **G, I, K** IIF of the AP membrane (ZO-1 in red) and RAB7A, RAB11, and RAB35, respectively (green). **H, J, L** Same images in the sagittal plane. Nuclei are blue labeled. White bars in (**A, C, E, G, I, K**) correspond to 25 μm, and in (**B, D, F, H, J, L**) to 20 μm. Quantitative confocal microscopy analysis of the proportion of BL (Na⁺K⁺ ATPase) and AP (ZO-1) markers co-localizing with RAB7A (**M**), RAB11A (**N**), and RAB35 (**O**). Quantitative confocal microscopy analysis of the proportion of RAB7A (**P**), RAB11A (**Q**), and RAB35 (**R**) co-localizing with the BL (Na⁺K⁺ ATPase) and AP (ZO-1) markers. Quantitative analyses were done using an average of $n = 12$ images from $n = 3$ independent biological replicates. The total number of cells counted was in the range of 600. Significant differences are shown.
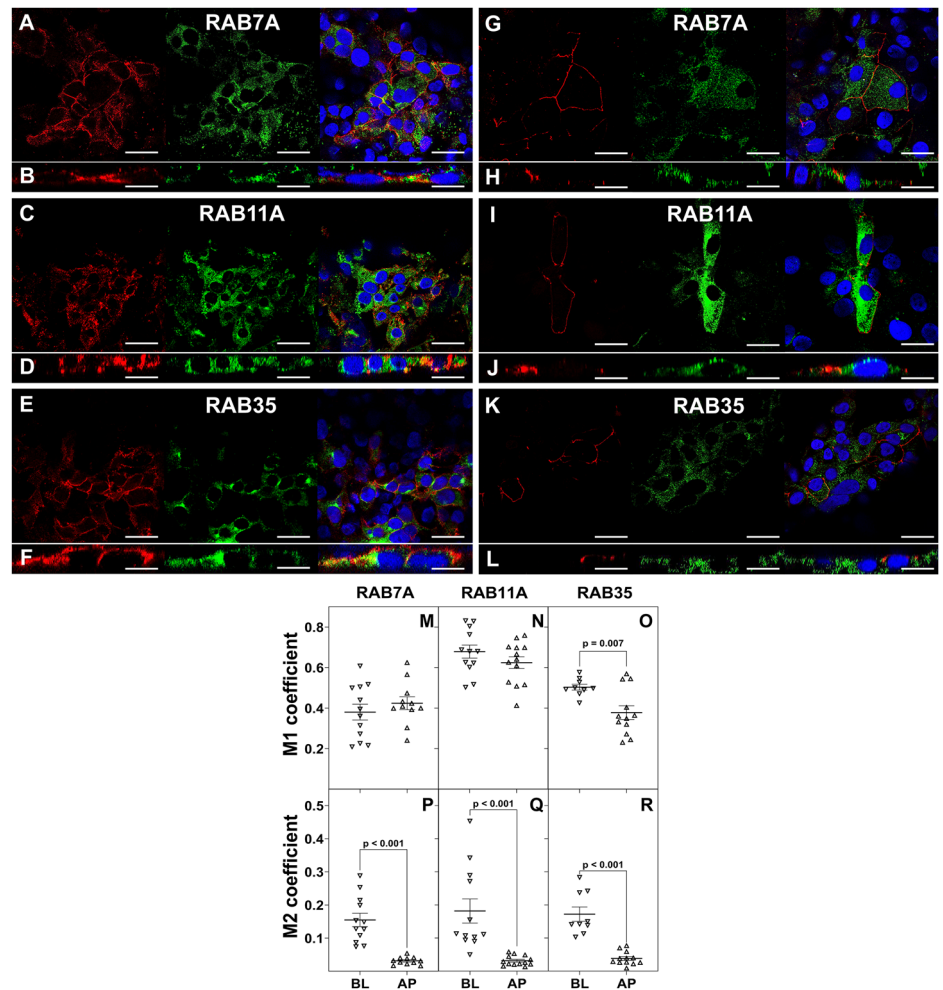
preferably use the ESCRT-mediated pathway, as previously described[25], while HP will preferentially use the syndecan-syntenin-ALIX-mediated pathway for capsid quasi-envelopment. Although it should not be ruled out a certain bias in this latter case, due to the high expression of syntenin-1 in hepatoma cells[37], this should be the same for the L0 and HP strains. Being not the case, it re-enforces the idea of the enhanced interaction of HP capsids with ALIX, through the VP2 S134G replacement, and the concurrent use of the syndecan-syntenin-ALIX-mediated exosome biogenesis pathway.

In close relationship with exosome biogenesis, we tried to identify which RAB GTPases could play a role in the eHAV-containing MVB trafficking, among those that had been previously recognized to be involved in exosome secretion[3–5] and expressed in Huh7-A-I cells. RAB35 was identified as the most critical GTPase for the egress of L0, and particularly of HP. Despite RAB7A is enriched in eHAV exosomes, it was previously discarded to be functional in eHAV egress[20], and this observation agrees with our results of single silencing. However, the information provided in double-silencing experiments revealed a certain role of RAB7A and RAB11A in eHAV egress, particularly for the L0 strain.

To identify whether the different uses of the exosome biogenesis/traffic pathways had any consequences on the cell cycle of L0 and HP strains, the kinetics of apical and basolateral egress of both strains were analyzed. The HP strain egressed similarly through both membranes, while the L0 strain showed a significantly higher release through the apical membrane. The reduced basolateral virus egress that we observed with both L0 and HP strains, compared with previous studies[32,38,39] may be explained by the distinct experimental designs used. However, in the present study, we compared the basolateral egress of L0 and HP strains, in parallel and under the same conditions. Additionally, the abundance of RAB7A, RAB11A, and RAB35 GTPases in the apical and basolateral membranes of polarized Huh7-A-I cells was also analyzed, and indicated that RAB35 was preferably located at the basolateral membrane.

In summary, the HP strain shows an enhanced ALIX interaction, preferentially using RAB35, which is more abundant in the basolateral membrane, and egresses through the basolateral membrane more efficiently than L0. In this context, we propose that L0 and HP strains may use hepatocyte compartments differently for the biogenesis and egress of the quasi-enveloped particles (Fig. 9). L0 would mostly use the ARE compartment, and in a lower proportion, the SAC. From the ARE compartment, using the ESCRT-mediated exosome biogenesis pathway MVBs will be formed, which would traffic to the apical membrane, controlled by RAB35, RAB7A and RAB11A GTPases, promoting the L0 eHAV particles egress; similarly, from the SAC compartment and controlled by RAB7A and RAB35, they would egress through the basolateral membrane. In contrast, HP strain would mostly use the SAC compartment, from which eHAV particles would traffic towards the apical membrane under RAB35, RAB7A, and RAB11A control. Also, from the BEE compartment and using the syndecan-syntein-ALIX-mediated exosome biogenesis pathway, eHAV particles from the HP strain would move to the basolateral membrane under RAB35 control. RAB35 has been described to control the fast-recycling pathway, from peripheral endocytic compartments to the plasma membrane, during receptor recycling, immunological synapse formation, and cytokinesis[40,41]. Fast recycling has been estimated to have a half time of <5 min[42]. During the HIV budding, the interaction of ALIX with a wild-type gag late domain shows a residence time of 45 ± 30 s, while the interaction with a mutant gag late domain requires repeated recruitments occurring every 4 ± 3 min[43]. Thus, it is tempting to speculate that the combination of
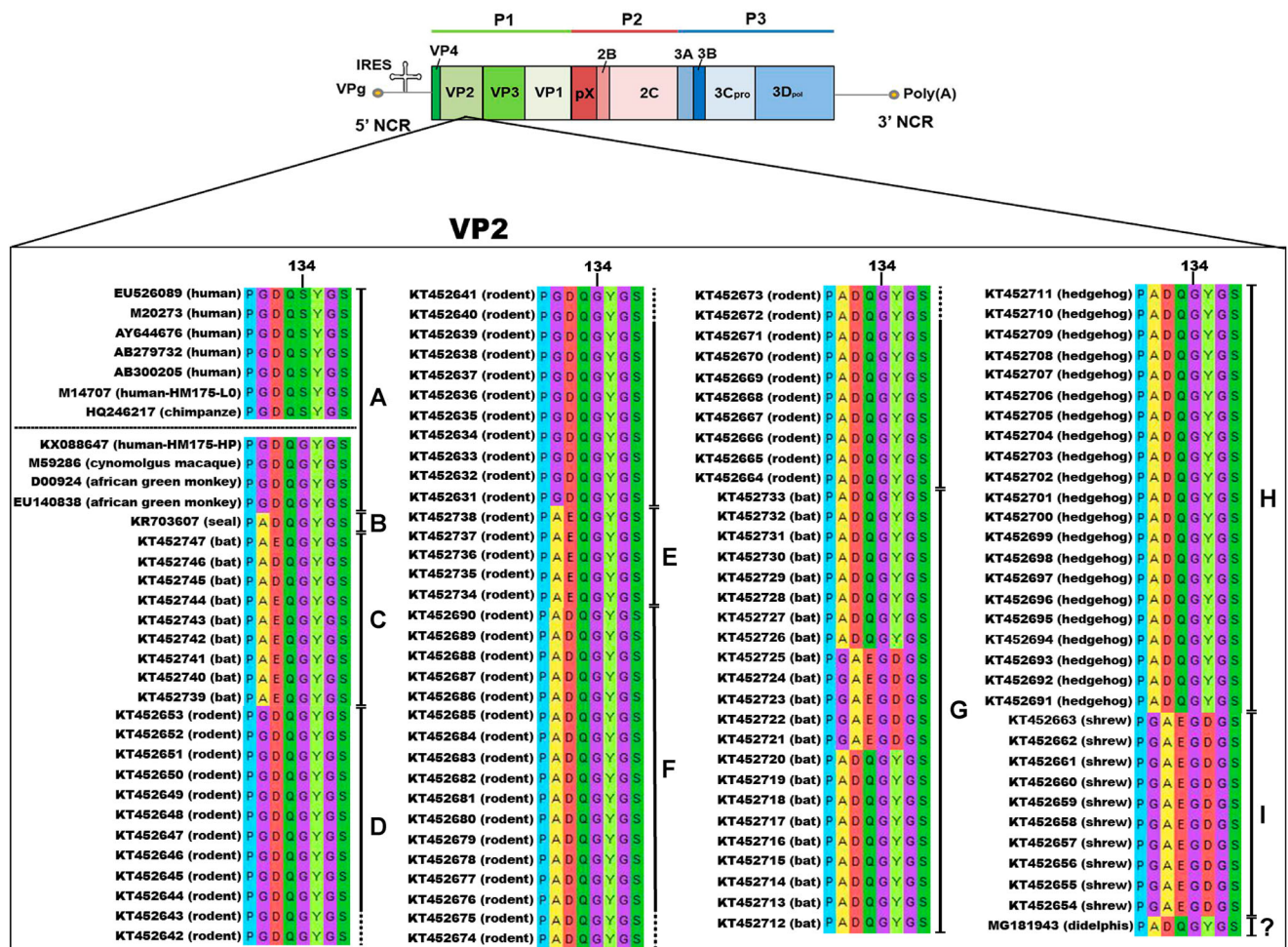
Fig. 8 | Phylogenetic conservation of residue 134 of VP2 in nine hepatovirus species infecting different mammalian species. A scheme of the HAV genome is illustrated above the alignment. Position 134 of VP2 is indicated by a vertical black line. Residues are colored following the Mega color scheme (A in yellow, E and D in red, G in magenta, Y in light green, Q and S in green, and P in blue). The alignment was constructed using 132 sequences from the nine existing *Hepatovirus* species, plus an still unclassified virus, infecting 34 different mammalian species (**A**: *Hepatovirus ahepa* infecting apes and monkeys; **B**: *Hepatovirus bephopi* infecting seals; **C**: *Hepatovirus cemanavi* infecting bats; **D**: *Hepatovirus devoli* infecting rodents; **E**: *Hepatovirus erubebrufu* infecting rodents; **F**: *Hepatovirus fejalco* infecting rodents; **G**: *Hepatovirus gafrisheta* infecting bats; **H**: *Hepatovirus hedgi* infecting hedgehogs; I: *Hepatovirus ishrewi* infecting shrews and **?**: an unclassified Hepatovirus infecting a marsupial) available at GenBank (EU526089, M20273.1, AY644676, AB279732, AB300205, M14707, HQ246217, KX088647, M59286, D00924, EU140838, KR703607, MG181943, KT452631-KT452747). The first seven sequences, belonging to hepatoviruses infecting humans and chimpanzees, show an S at position 134. The human HP strain represents an exception and aligns with sequences from monkeys and small mammals.

the fast-growing phenotype with an enhanced ALIX interaction could permit HP to be at the right place (basolateral periphery) at the right time (coupling the exosome biogenesis at the BEE with the fast recycling). Additionally, RAB7A, RAB11A, and RAB35 have also been involved in the slow endosome recycling[44–46], and the former two have been described to play a role in the extracellular release of hepatitis C virus[47–49]. Additionally, RAB27A has been reported to promote hepatitis C and E viruses release[50,51], and although we cannot rule out a role in the HAV release, its mRNA levels do not increase during HAV infection. The proposed model is very speculative, and other pathways may be envisaged depending on the use of peripheral or perinuclear lysosome populations for virus uncoating, which will determine the localization of virus replication and assembly[52].

Other amino acid replacements are present in the coding region for the non-structural proteins of the HP strain. Thus, we cannot completely rule out their effect on capsid morphogenesis, and in consequence, on the interaction with ALIX. Specifically, a replacement in 2C (R54K), a second one in the 3C protease (Q106K), and another in the 3D polymerase (A39V). All these proteins are intimately associated with membranes and are mostly involved in viral replication rather than in morphogenesis[53]. Considering that HP also harbors three mutations in the IRES, which significantly

increase its activity[34,54], it may be hypothesized that all these mutations act epistatically, resulting in the fast-growing phenotype of HP. Finally, since the L123F replacement in the VP1 protein is located far from the late domains in the capsid[22], we postulate the S134G replacement in VP2 as the most significant for the HP-ALIX interaction enhancement. Ultimately, the HP strain more effectively engages the syndecan-syntenin-ALIX-mediated exosome biogenesis pathway, allowing for more efficient egress through the basolateral membrane than the L0 strain, which utilizes this pathway to a lesser extent.

Since the S134G replacement has not been previously described in human HAV strains, we wondered if it could occur in other hepatoviruses. Interestingly, all hepatoviruses infecting apes, including humans and chimpanzees, have Serine, while those infecting monkeys, seals, rodents, hedgehogs, shrews, bats and marsupials have Glycine. The meaning of such a pattern is unknown, but it could be related to the strong immune function in primates[55]. Apes mount a stronger early transcriptional response to viral infections than monkeys, including interferon (IFN) alpha and gamma responses. Intrahepatic plasmacytoid dendritic cells (pDCs) are transiently present at the beginning of the HAV infection in chimpanzees[56]. Moreover, pDCs stimulated in vitro with quasi-enveloped eHAV virions, in the

Fig. 9 | Diagram of the differential egress of hepatitis A virus (HAV) through the apical and basolateral membranes of hepatocytes. Three ALIX-interacting domains exist in the HAV capsid: one located in the pX domain[25], and the others in the VP2 late domains[21]. The pX domain is highly accessible, and it is present in L0 and HP HAV strains. Using this domain, both strains interact with the HD-PTP and ALIX Bro1 domains, promoting an ESCRT-dependent entry into multivesicular bodies (MVB)[25], likely derived from the apical recycling endosomes (ARE) and the subapical endosome compartment (SAC). These MVBs traffic towards the apical membrane using RAB35, RAB7A, and RAB11A or to the basolateral membrane using RAB35 and RAB7A. The VP2 late domains are less accessible, but the replacement S134G, present in the HP strain, facilitates the interaction of one of its late domains with ALIX V domains. This interaction would promote the internalization of HP capsids into MVBs derived from the basolateral early endosomes (BEE) using the syndecan-syntenin-ALIX-exosome biogenesis pathway. These MVBs will traffic towards the basolateral membrane mostly using RAB35. The L0 strain may also use this pathway, although less efficiently. Created in BioRender. https://BioRender.com/seownnd.
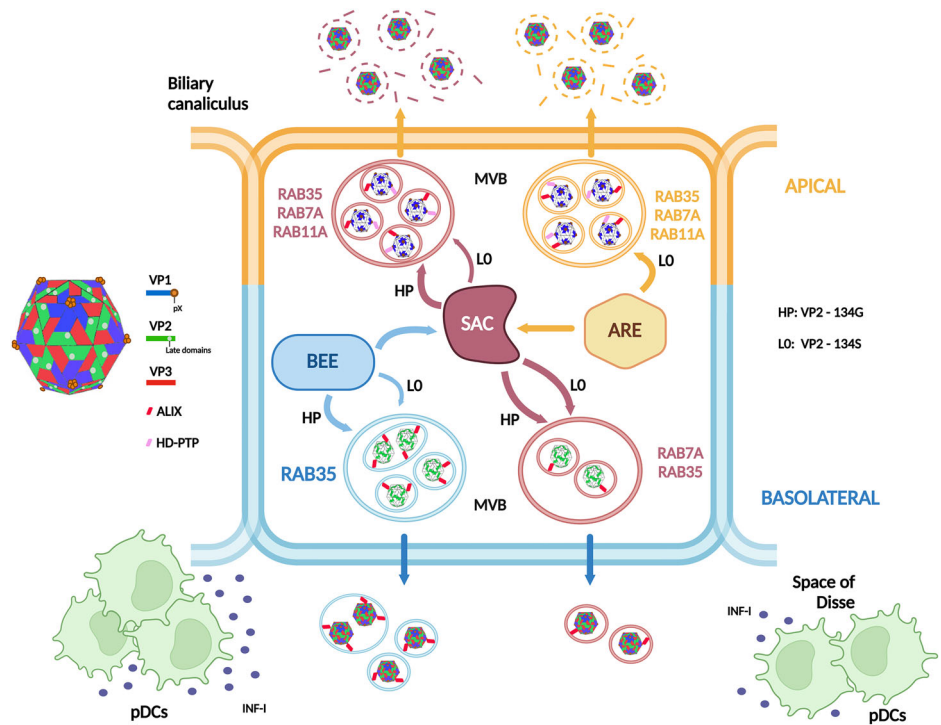
absence of replication, produce substantial amounts of IFN-α[56]. Therefore, hepatoviruses infecting apes might have evolved to minimize contact with the pDCs by replacing Gly at position 134 of VP2 by Ser, which reduces the basolateral egress. Yet, there is no data on the antiviral response elicited against hepatovirus infections in monkeys and small mammals, capable of confirming our hypothesis.

Methods
Viruses and cells
Two cell-culture adapted HAV variants derived from the HM-175 strain[57] were used throughout this study: the HM-175-43c variant[33], i.e., L0, and the fast-growing HM-175-HP variant[34,54], i.e., HP, with GenBank accession numbers KF724017 and KX088647[34,54], respectively.

Virus stocks were produced infecting FRhK-4 cells (kindly provided by the late Professor Bertram Flehmig from the University of Tübingen, Germany) with a MOI of 0.1. Cells were grown in minimal essential medium in the presence of non-essential amino acids and L-glutamine and supplemented with 15% fetal calf serum (FCS). Post-infection (p.i.) media contained 2% FCS. For HP, 0.05 μg/ml of actinomycin D (AMD; Sigma) was added in the p.i. media to induce a 60-70% inhibition of the cell DNA transcription and thus promoting the cell shutoff[58].

In the experiments included in this study, HAV strains were replicated in the human hepatocarcinoma-derived Huh7-A-I cell line[35] (kindly provided by Dr Gerardo Kaplan from the FDA, US), in which they are non-cytopathic. In this case, growth media contained 10% of FCS, and no AMD was added for HP replication. Virus inoculum used throughout this study consisted of supernatants of infected FRhK-4 cells, which contained mostly eHAV particles (90% and over 95% for L0 and HP strains, respectively)[54].

Virus and genome titration
Tissue Culture Infectious Dose 50 (TCID$_{50}$) titers were determined by infecting microtiter plates of FRhK-4 cells with serial ten-fold dilutions of virus supernatants in the absence of AMD[59]. The development of HAV-induced cytopathic effect was assessed at 10–13 days p.i.

HAV GC numbers were determined by Real-Time-qPCR[60] using the RNA UltraSense One-Step Quantitative RT-PCR System (Invitrogen).

Virus purification through iodixanol gradients and electron microscopy
Purification of naked and quasi-enveloped viruses was performed as previously described[1,54]. Briefly, supernatants from infected Huh7-A-I were centrifuged at $1500 \times g$ for 10 min at 4 °C to remove cellular debris, and supernatants were further clarified by centrifuging twice at $10,000\,g$ for 30 min at 4 °C. Viruses were concentrated by ultracentrifugation at $100,000 \times g$ for 2 h at 4 °C, pellets resuspended in 1 ml of PBS and loaded onto pre-formed 6%–50% iodixanol-(OptiPrep, Axis-Shield) in 0.3 M sucrose gradients, which were centrifuged at $205,000 \times g$ for 2 h and 45 min at 4 °C (SW41 Ti rotor in a Beckman Coulter Optima L-90K centrifuge). Twenty 0.5 ml fractions were collected, and their density was determined using a refractometer. RNA was extracted from each fraction using the Nucleospin RNA Virus Extraction Kit (Macherey-Nagel), and HAV GC numbers were determined.

Three virus stocks of L0 and HP strains were produced by infecting T-75 flasks of Huh7-A-I cells, using a MOI of 1, for 7 days, gradient purified, and the proportion of naked and quasi-enveloped viruses analyzed. For electron microscopy, pools of fractions corresponding to naked and quasi-enveloped particles were submitted to dialysis for 3 days against TN buffer (50 mM Tris, 100 mM NaCl) with changes every 12 h to remove iodixanol and sucrose. Samples were ultracentrifuged at $100,000 \times g$ for 3 h at 4 °C, and pellets resuspended in 25 μl of PBS. After negative staining with 2% phosphotungstic acid pH 7.3, samples were observed with a JEOL JEM 1010 (Jeol) electron microscope at 80 kV. Images were taken with the Megaview III charge-coupled device camera at 1000×1000 pixels and analyzed with the AnalySIS version 3.2 software (Olympus Soft Imaging Solutions).

Gene expression analysis by mRNA relative quantification
Expression of genes coding for ALIX, HD-PTP, TSG101, syntenin-1, syndecan 1, RAB7A, RAB11A, RAB11C, RAB27A, RAB27B, and RAB35 was analyzed in Huh7-A-I cells at 24, 48, and 72 h after confluence. Six independent biological replicates were performed, each including two technical replicates, whose average was used for calculations. Cells were seeded at a ratio of 5×10^5 in T-25 flasks and grown at 37 °C under 5% CO_2 for 48 h to reach confluence.

Additionally, confluent cells were infected with L0 and HP strains using an MOI of 5, and gene expression re-analyzed. Mock-infected cells were used as negative controls. Six independent biological replicates were performed for each population and p.i. time, each with two technical replicates. The average of the two technical replicates was used for calculations. For gene expression analysis, cells were lysed at 24, 48 and 72 h p.i.

Total RNA from lysates was extracted with GenElute™ Mammalian Total RNA Miniprep Kit (Sigma-Aldrich) following the manufacturer's instructions. A RT-qPCR using the KiCqStart® One-Step Probe RT-qPCR ReadyMix™ kit (Sigma-Aldrich) with pre-designed primers and probes from KiCqStart® Probe Assays (Sigma-Aldrich; Supplementary Table 3) was performed. Glyceraldehyde-3-phosphate dehydrogenase (GAPDH) expression was ascertained in each sample as an endogenous reference[61]. Relative gene expression was determined as previously described[62]. Summarizing, target Cq values were normalized vs GAPDH, and then differences between HAV-infected and mock-infected cells were ascertained. A minimum of a ±2-fold-change was established as a cutoff level[63]. Additionally, virus replication was confirmed by determining GC numbers in the supernatant at 0, 24, 48, and 72 h p.i., as described above. Total RNA from the supernatants was purified as described above.

Gene silencing
Around 6.5×10^4 Huh7-A-I cells per well were seeded on 24-well plates and grown for 24 h at 37 °C under 5% CO_2 to reach 70-80% confluence. Transfection of siRNA sequence mixtures targeting the *PDCD6IP* (ALIX), *PTPN23* (HD-PTP), *SDCBP* (syntenin-1), *RAB7A*, *RAB11A*, and *RAB35* genes was performed to knock down their individual or dual expression. The SMART pool ON-TARGETplus siRNA system (Dharmacon, GE Healthcare) was employed according to the manufacturer's instructions. For RAB genes, double-silencing experiments were performed combining siRNA mixtures. A non-targeting (NT) siRNA mixture was used as negative control. At 48 h after transfection, cells were infected with L0 and HP strains using an MOI of 5. Mock-infected cells were used as negative controls. A minimum of six biological replicates were performed for each gene silencing and HAV population. Each biological replicate included two technical replicates, whose average was used for further analysis.

Supernatants and cell lysates were collected at 24 h p.i. Virus titers in the supernatants were expressed as $TCID_{50}$. Total RNA was extracted from cell lysates and used for titration of virus GC and mRNA expression. Both $TCID_{50}$ and GC were twice titrated (technical replicates), and the average was used for further calculations. Specific gene silencing was assessed by calculating the relative gene expression using the method mentioned above. Additionally, western blots of cell extracts for the detection of ALIX, HD-PTP, syntenin-1, the different RAB GTPases, and GAPDH, as a normalization control, were performed with the antibodies described in Supplementary Table 4.

The effect of gene silencing on L0 and HP egress was assessed by comparing the infectious viral loads in the supernatants and the intracellular GC numbers in knockdown vs non-knockdown cells, as previously described[1]. Additionally, the ratio of the total intracellular GC to the total extracellular $TCID_{50}$ in non-silenced and silenced cells was calculated and used as a measure of virus egress. In confocal microscopy knock-down experiments, cells were fixed at 24 h p.i. and processed for immunofluorescence as described below.

Confocal microscopy
Huh7-A-I cell monolayers grown on chambered coverglasses (Lab-Tek® Chambered 1.0 Borosilicate Coverglass System Nunc™, Thermo Scientific™) were infected using a MOI of 5. At 24, 48, or 72 h p.i., cells were fixed with 4% paraformaldehyde (PFA) for 15 min, permeabilized with 0.5% Triton X-100 in PBS with 20 mM glycine for 10 min, and blocked with 1% bovine serum albumin in PBS-glycine for 30 min, with all steps performed at room temperature. Antigen detection with the corresponding antibodies (Supplementary Table 4) was done at 37 °C for 1 h, and after two washes, cells were incubated with secondary antibodies at 37 °C for 1 h. Nuclei were Hoechst-stained (Supplementary Table 4) for 15 min. Images were captured

on Leica TCS SP2 and Zeiss 880 confocal microscopes with a 63× 1.4 NA objective, obtaining 8-bit and 16-bit images with resolutions of 0.1, 0.1, 0.5 microns and 0.07, 0.07, 0.5 microns, respectively. Image deconvolution was performed with Huygens Essential v. 3.7.1. ImageJ v1.54 g software was used to calculate the Otsu threshold for a subset of three representative images of each experimental condition, and a mean threshold value for each of the two channels (red and green) was obtained. 3D co-localization analyses were performed using Huygens Essential, applying the previously calculated thresholds. 2D reconstructed images used in the figures were obtained with ImageJ, maintaining the previously calculated thresholds.

Mander's co-localization Coefficients (M1 and M2) were used for the quantitative analysis. A minimum of two independent biological replicates were performed, and a minimum of four representative captures were taken for each replicate. An average of 50 cells per image was analyzed.

HAV immunoprecipitation
For immunoprecipitation experiments, viral capsids were obtained from supernatants of infected cells submitted to three cycles of freeze-thawing, plus three 30 s cycles of sonication at 60 W. Three different stocks were prepared. One-ml samples containing around 5×10^3 $TCID_{50}$ units were incubated for 2 h at room temperature with a non-infected clarified cell extract at a 1:1 proportion, and subsequently immunoprecipitated with an anti-HAV monoclonal antibody or an anti-ALIX polyclonal antibody (Supplementary Table 4) coupled with magnetic Protein G Dynabeads (Invitrogen) following the manufacturer's procedure. Immunoprecipitated and non-immunoprecipitated viruses were titrated by RT-qPCR as described above. Titers obtained after immunoprecipitation with the anti-HAV antibody were given a value of 100%, and titers obtained after co-immunoprecipitation with the anti-ALIX were expressed relative to this percentage. Four independent biological replicates were assayed.

Huh7-A-I polarization
Huh7-A-I cells were seeded at a ratio of $4.5 \times 10^5/cm^2$ on polycarbonate transwell 0.4 μm inserts (Corning™ Transwell® 12-well plate), on coverglasses (Lab-Tek® Chambered 1.0 Borosilicate Coverglass System Nunc™ 8 well plate, Thermo Scientific™), or on T-25 flasks. Minimal essential medium containing non-essential amino acids and 15% FCS was used for cell growth. When the confluence was reached, around 5 days after seeding, growth media supplemented with 1% dimethyl sulfoxide (DMSO; Sigma-Aldrich) was refreshed every other day for 10 days.

Polarization status was confirmed by confocal analysis of cells grown on coverslips after labeling with an anti-Na$^+$K$^+$ ATPase mouse mAb antibody and an anti-Z0-1 rabbit polyclonal antibody (Supplementary Table 4) as markers for the basolateral and apical membranes, respectively. The percentage of permeability of monolayers of cells grown on transwells was assessed by a fluorescent dextran assay and used as an additional polarization marker. Cells were incubated for 24 h with 5 mM 4 KDa FITC-dextran (Sigma-Aldrich) added through the apical compartment. Fluorescence in the apical and basolateral compartments was quantified using a standard curve from 6.125 nM to 2.5 μM concentration, using a spectrofluorometer. Four independent biological replicates were performed.

Virus infections in polarized Huh7-A-I cells grown in transwells
Polarized Huh7-A-I cell monolayers grown on 12-well transwells were used to test the vectorial release of the L0 and HP strains.

To test virus transcytosis, infections through the basolateral or the apical compartments with an MOI of 5 were performed. After a 90-min adsorption, the inoculum was removed, and the monolayers were washed twice with p.i. media. Finally, infected cells were incubated with 1-ml of p.i. media. Supernatant samples were collected at hourly intervals for 3 h at 37 °C, with cells re-fed with fresh medium. Six independent biological replicates were conducted, each containing two technical replicates. The average of the technical replicates was used for further calculations.

For the analysis of virus production, cells were basolaterally infected with a MOI of 5, and samples from both the apical and basolateral

compartments were collected at 2, 5, and 7 days p.i. Residual virus titers at day 0 p.i. in the media added after the adsorption washing were subtracted from titers obtained at days 2, 5, and 7 p.i. Nine independent biological replicates were performed. Each replicate was twice titrated in FRhK-4 cells as described above, and their average was used for calculations.

Amino acid sequence alignments

Constraint-based amino acid alignment from 132 VP2 sequences from the 9 existing hepatovirus species (https://ictv.global/report/chapter/picornaviridae/picornaviridae/hepatovirus), infecting 34 different mammalian species[64–66] available at GenBank (EU526089, M20273.1, AY644676, AB279732, AB300205, M14707.1, HQ246217, KX088647, M59286, D00924, EU140838, KR703607, MG181943, KT452631-KT452747) was performed. Similarly, 28 VP1 sequences (EU526089, M20273, AY644676, AB279732, AB300205, HQ246217, M14707, KX088647, M59286, D00924, EU140838, NC_027818, KR703607, MG181943, KT452637, KT452641, KT452644, KT452658, KT452661, KT452685, KT452691, KT452695, KT452698, KT452714, KT452729, KT452730, KT452735, KT452742) were also analyzed. Alignments were produced using Mega v11[67].

Statistics and reproducibility

The Shapiro-Wilk test was used to analyze the normal distribution of the variables ($p > 0.05$), and the Brown–Forsythe test was used as an equal variance test ($p > 0.05$). When normal distribution was not fulfilled, the Mann-Whitney test was automatically applied. Also, when the homoscedasticity was not reached, the Welch's correction was automatically computed. The Student's t-test (unpaired two-tailed) was performed to compare pairs of results. For multiple comparisons, one-way ANOVA with the recommended correction tests was applied. The statistical analysis was conducted at a 95% confidence level. All statistical analyses and graphs were performed using the GraphPad v10.2.3 software.

For reproducibility, several independent biological replicates were used, including several technical replicates, i.e., two RT-qPCR and TCID$_{50}$ measurements and twelve images in confocal quantitative analysis. The specific numbers are indicated in each of the experimental procedures described above as well as in the figure legends.

Reporting summary

Further information on research design is available in the Nature Portfolio Reporting Summary linked to this article.

Data availability

Complete data are available in the main article and the Supplementary Materials and Supplementary Data document.

References

1. Feng, Z. et al. A pathogenic picornavirus acquires an envelope by hijacking cellular membranes. *Nature* **496**, 367–371 (2013).
2. Feng, Z., Hirai-Yuki, A., McKnight, K. L. & Lemon, S. M. Naked viruses that aren't always naked: quasi-enveloped agents of acute hepatitis. *Annu. Rev. Virol.* **1**, 539–560 (2014).
3. Colombo, M., Raposo, G. & Théry, C. Biogenesis, secretion, and intercellular interactions of exosomes and other extracellular vesicles. *Annu. Rev. Cell Dev. Biol.* **30**, 255–289 (2014).
4. Hessvik, N. P. & Llorente, A. Current knowledge on exosome biogenesis and release. *Cell Mol. Life Sci.* **75**, 193–208 (2018).
5. Blanc, L. & Vidal, M. New insights into the function of Rab GTPases in the context of exosomal secretion. *Small GTPases* **9**, 95–106 (2018).
6. Hurley, J. H. ESCRTs are everywhere. *Embo J.* **34**, 2398–2407 (2015).
7. Hurley, J. H. & Odorizzi, G. Get on the exosome bus with ALIX. *Nat. Cell Biol.* **14**, 654–655 (2012).
8. Zimmermann, P. et al. PIP(2)-PDZ domain binding controls the association of syntenin with the plasma membrane. *Mol. Cell* **9**, 1215–1225 (2002).
9. Baietti, M. F. et al. Syndecan–syntenin–ALIX regulates the biogenesis of exosomes. *Nat. Cell Biol.* **14**, 677 (2012).
10. Dores, M. R. et al. ALIX binds a YPX(3)L motif of the GPCR PAR1 and mediates ubiquitin-independent ESCRT-III/MVB sorting. *J. Cell Biol.* **197**, 407–419 (2012).
11. McCullough, J., Fisher, R. D., Whitby, F. G., Sundquist, W. I. & Hill, C. P. ALIX-CHMP4 interactions in the human ESCRT pathway. *Proc. Natl. Acad. Sci. USA* **105**, 7687–7691 (2008).
12. Dussupt, V. et al. The nucleocapsid region of HIV-1 Gag cooperates with the PTAP and LYPXnL late domains to recruit the cellular machinery necessary for viral budding. *PLoS Pathog.* **5**, e1000339 (2009).
13. Ren, X. & Hurley, J. H. Proline-rich regions and motifs in trafficking: from ESCRT interaction to viral exploitation. *Traffic* **12**, 1282–1290 (2011).
14. Morita, E. & Sundquist, W. I. Retrovirus budding. *Annu. Rev. Cell Dev. Biol.* **20**, 395–425 (2004).
15. Zhai, Q. et al. Structural and functional studies of ALIX interactions with YPX(n)L late domains of HIV-1 and EIAV. *Nat. Struct. Mol. Biol.* **15**, 43–49 (2008).
16. Fisher, R. D. et al. Structural and biochemical studies of ALIX/AIP1 and its role in retrovirus budding. *Cell* **128**, 841–852 (2007).
17. Martin-Serrano, J. & Neil, S. J. Host factors involved in retroviral budding and release. *Nat. Rev. Microbiol.* **9**, 519–531 (2011).
18. Sette, P. et al. HIV-1 Nucleocapsid mimics the membrane adaptor syntenin PDZ to gain access to ESCRTs and promote virus budding. *Cell Host Microbe* **19**, 336–348 (2016).
19. Fujii, K., Hurley, J. H. & Freed, E. O. Beyond Tsg101: the role of Alix in 'ESCRTing' HIV-1. *Nat. Rev. Microbiol.* **5**, 912–916 (2007).
20. McKnight, K. L. et al. Protein composition of the hepatitis A virus quasi-envelope. *Proc. Natl. Acad. Sci. USA* **114**, 6587–6592 (2017).
21. Gonzalez-Lopez, O. et al. Redundant late domain functions of tandem VP2 YPX(3)L motifs in nonlytic cellular egress of quasi-enveloped hepatitis A virus. *J. Virol.* **92**, e01308–e01318 (2018).
22. Wang, X. et al. Hepatitis A virus and the origins of picornaviruses. *Nature* **517**, 85–88 (2015).
23. Pires, R. et al. A crescent-shaped ALIX dimer targets ESCRT-III CHMP4 filaments. *Structure* **17**, 843–856 (2009).
24. Odorizzi, G. The multiple personalities of Alix. *J. Cell Sci.* **119**, 3025–3032 (2006).
25. Shirasaki, T. et al. Nonlytic cellular release of hepatitis A virus requires dual capsid recruitment of the ESCRT-associated Bro1 domain proteins HD-PTP and ALIX. *PLoS Pathog.* **18**, e1010543 (2022).
26. Treyer, A. & Musch, A. Hepatocyte polarity. *Compr. Physiol.* **3**, 243–287 (2013).
27. Schulze, R. J., Schott, M. B., Casey, C. A., Tuma, P. L. & McNiven, M. A. The cell biology of the hepatocyte: a membrane trafficking machine. *J. Cell Biol.* **218**, 2096–2112 (2019).
28. Tauro, B. J. et al. Two distinct populations of exosomes are released from LIM1863 colon carcinoma cell-derived organoids. *Mol. Cell. Proteom.* **12**, 587–598 (2013).
29. Mittelbrunn, M., Vicente Manzanares, M. & Sanchez-Madrid, F. Organizing polarized delivery of exosomes at synapses. *Traffic* **16**, 327–337 (2015).
30. Ostrowski, M. et al. Rab27a and Rab27b control different steps of the exosome secretion pathway. *Nat. Cell Biol.* **12**, 19–30 (2010). sup pp 11-13.
31. Wakabayashi, Y., Dutt, P., Lippincott-Schwartz, J. & Arias, I. M. Rab11a and myosin Vb are required for bile canalicular formation in WIF-B9 cells. *Proc. Natl. Acad. Sci. USA* **102**, 15087–15092 (2005).
32. Hirai-Yuki, A., Hensley, L., Whitmire, J. K. & Lemon, S. M. Biliary secretion of quasi-enveloped human hepatitis A virus. *mBio* **7**, e01998–16 (2016).

33. Cromeans, T., Fields, H. A. & Sobsey, M. D. Replication kinetics and cytopathic effect of hepatitis A virus. *J. Gen. Virol.* **70**, 2051–2062 (1989).

34. Perez-Rodriguez, F. J. et al. Improving virus production through quasispecies genomic selection and molecular breeding. *Sci. Rep.* **6**, 35962 (2016).

35. Konduru, K. & Kaplan, G. Stable growth of wild-type hepatitis A virus in cell culture. *J. Virol.* **80**, 1352–1360 (2006).

36. Gissen, P. & Arias, I. M. Structural and functional hepatocyte polarity and liver disease. *J. Hepatol.* **63**, 1023–1037 (2015).

37. Liu, X., Zhang, X., Lv, Y., Xiang, J. & Shi, J. Overexpression of syntenin enhances hepatoma cell proliferation and invasion: potential roles in human hepatoma. *Oncol. Rep.* **32**, 2810–2816 (2014).

38. Dao Thi, V. L. et al. Stem cell-derived polarized hepatocytes. *Nat. Commun.* **11**, 1677 (2020).

39. Snooks, M. J. et al. Vectorial entry and release of hepatitis A virus in polarized human hepatocytes. *J. Virol.* **82**, 8733–8742 (2008).

40. Kouranti, I., Sachse, M., Arouche, N., Goud, B. & Echard, A. Rab35 regulates an endocytic recycling pathway essential for the terminal steps of cytokinesis. *Curr. Biol.* **16**, 1719–1725 (2006).

41. Patino-Lopez, G. et al. Rab35 and its GAP EPI64C in T cells regulate receptor recycling and immunological synapse formation. *J. Biol. Chem.* **283**, 18323–18330 (2008).

42. Jonker, C. T. H. et al. Accurate measurement of fast endocytic recycling kinetics in real time. *J. Cell Sci.* **133**, jcs231225 (2020).

43. Gupta, S., Bendjennat, M. & Saffarian, S. Abrogating ALIX interactions results in stuttering of the ESCRT machinery. *Viruses* **12**, 1032 (2020).

44. Girard, E. et al. Rab7 is functionally required for selective cargo sorting at the early endosome. *Traffic* **15**, 309–326 (2014).

45. Lock, J. G. & Stow, J. L. Rab11 in recycling endosomes regulates the sorting and basolateral transport of E-cadherin. *Mol. Biol. Cell* **16**, 1744–1755 (2005).

46. Grant, B. D. & Donaldson, J. G. Pathways and mechanisms of endocytic recycling. *Nat. Rev. Mol. Cell Biol.* **10**, 597–608 (2009).

47. Coller, K. E. et al. Molecular determinants and dynamics of hepatitis C virus secretion. *PLoS Pathog.* **8**, e1002466 (2012).

48. Bayer, K., Banning, C., Bruss, V., Wiltzer-Bach, L. & Schindler, M. Hepatitis C virus is released via a noncanonical secretory route. *J. Virol.* **90**, 10558–10573 (2016).

49. Elgner, F. et al. The intracellular cholesterol transport inhibitor U18666A inhibits the exosome-dependent release of mature hepatitis C virus. *J. Virol.* **90**, 11181–11196 (2016).

50. Shrivastava, S. et al. Knockdown of autophagy inhibits infectious hepatitis C virus release by the exosomal pathway. *J. Virol.* **90**, 1387–1396 (2016).

51. Nagashima, S. et al. Hepatitis E virus egress depends on the exosomal pathway, with secretory exosomes derived from multivesicular bodies. *J. Gen. Virol.* **95**, 2166–2175 (2014).

52. Pu, J., Guardia, C. M., Keren-Kaplan, T. & Bonifacino, J. S. Mechanisms and functions of lysosome positioning. *J. Cell Sci.* **129**, 4329 (2016).

53. McKnight, K. L. & Lemon, S. M. Hepatitis A virus genome organization and replication strategy. *Cold Spring Harb. Perspect. Med.* **8**, a03348 (2018).

54. Chavarria-Miro, G. et al. Advances for the hepatitis A virus antigen production using a virus strain with codon frequency optimization adjustments in specific locations. *Front. Microbiol.* **12**, 642267 (2021).

55. Hawash, M. B. F. et al. Primate innate immune responses to bacterial and viral pathogens reveals an evolutionary trade-off between strength and specificity. *Proc. Natl. Acad. Sci. USA* **118**, e2015855118 (2021).

56. Feng, Z. et al. Human pDCs preferentially sense enveloped hepatitis A virions. *J. Clin. Investig.* **125**, 169–176 (2015).

57. Gust, I. D. et al. The origin of the HM175 strain of hepatitis A virus. *J. Infect. Dis.* **151**, 365–367 (1985).

58. Aragonès, L., Guix, S., Ribes, E., Bosch, A. & Pintó, R. M. Fine-tuning translation kinetics selection as the driving force of codon usage bias in the hepatitis A virus capsid. *PLoS Pathog.* **6**, e1000797 (2010).

59. Costafreda, M. I. et al. Hepatitis A virus adaptation to cellular shutoff is driven by dynamic adjustments of codon usage and results in the selection of populations with altered capsids. *J. Virol.* **88**, 5029–5041 (2014).

60. Costafreda, M. I., Bosch, A. & Pintó, R. M. Development, evaluation, and standardization of a real-time TaqMan reverse transcription-PCR assay for quantification of hepatitis a virus in clinical and shellfish samples. *Appl. Environ. Microbiol* **72**, 3846–3855 (2006).

61. Barber, R. D., Harmer, D. W., Coleman, R. A. & Clark, B. J. GAPDH as a housekeeping gene: analysis of GAPDH mRNA expression in a panel of 72 human tissues. *Physiol. Genom.* **21**, 389–395 (2005).

62. Schmittgen, T. D. & Livak, K. J. Analyzing real-time PCR data by the comparative C(T) method. *Nat. Protoc.* **3**, 1101–1108 (2008).

63. Mozūraitis, R. et al. Zika virus modulates human fibroblasts to enhance transmission success in a controlled lab-setting. *Commun. Biol.* **8**, 139 (2025).

64. Drexler, J. F. et al. Evolutionary origins of hepatitis A virus in small mammals. *Proc. Natl. Acad. Sci. USA* **112**, 15190–15195 (2015).

65. de Carvalho Dominguez Souza, B. F. et al. A novel hepatitis B virus species discovered in capuchin monkeys sheds new light on the evolution of primate hepadnaviruses. *J. Hepatol.* **68**, 1114–1122 (2018).

66. Anthony, S. J. et al. Discovery of a novel hepatovirus (phopivirus of seals) related to human hepatitis A virus. *mBio* **6**, e01180–15 (2015).

67. Tamura, K., Stecher, G. & Kumar, S. MEGA11: molecular evolutionary genetics analysis version 11. *Mol. Biol. Evol.* **38**, 3022–3027 (2021).

Author contributions

A.C., A.A., G.C., and M.dC. performed most of the experiments. A.C., A.B., and R.M.P. interpreted data and wrote the manuscript. C.F., D.G.P., A.M.V., and E.R. helped with all experiments. S.G., M.I.C., A.B., and R.M.P. conceptualized and supervised the study and reviewed the manuscript. All authors have read and approved the final manuscript.

Competing interests

The authors declare no competing interests.

Additional information

Supplementary information The online version contains supplementary material available at https://doi.org/10.1038/s42003-025-08344-w.

Correspondence and requests for materials should be addressed to Rosa M. Pintó.

Peer review information *Communications Biology* thanks the anonymous reviewers for their contribution to the peer review of this work. Primary Handling Editors: X Frank Zhang and Tobias Goris. A peer review file is available.

Reprints and permissions information is available at http://www.nature.com/reprints

Publisher's note Springer Nature remains neutral with regard to jurisdictional claims in published maps and institutional affiliations.